

Learning a robust shape parameter for RBF approximation

Maria Han Veiga¹ and Fatemeh Nassajian Mojarrad²

¹Department of Mathematics, Ohio State University

²Department of Computer Science, University of Geneva

Abstract

Radial basis functions (RBFs) play an important role in function interpolation, in particular in an arbitrary set of interpolation nodes. The accuracy of the interpolation depends on a parameter called the *shape parameter*. There are many approaches in literature on how to appropriately choose it as to increase the accuracy of interpolation while avoiding instability issues. However, finding the optimal shape parameter value in general remains a challenge. We present a novel approach to determine the shape parameter in RBFs: we introduce a data-driven method that controls the condition of the interpolation matrix to avoid numerically unstable interpolations, while keeping a very good accuracy. In addition, we formulate a fall-back procedure that enforces a strict upper bound on the condition number of the generated interpolation matrix. We present numerical test cases to assess the performance of the proposed methods in interpolation tasks and in a RBF based finite difference (RBF-FD) method, in one and two-space dimensions.

1 Introduction

Radial basis functions (RBFs) have a variety of applications, for example, in function approximation, function interpolation and numerical representation of solutions of partial differential equations (PDEs). The main advantages of using RBFs for interpolation are:

- RBFs¹ lead to a well-posed problems when interpolating on an arbitrary set of points of dimension $n \in \mathbb{N}$ (e.g.: chapter 6 [1]);
- Treating multi-dimensional problems is simple, as many RBFs are uni-dimensional functions of distance.

The interpolation problem reads: given data $\{x_i, f(x_i)\}_{i=1}^N$, with $x_i \in \mathbb{R}^n$ and $f(x_i) \in \mathbb{R}$, one wishes to find an interpolation function s such that $s(x_i) = f(x_i)$ for all i . Using RBFs, we seek the approximating function s of the form:

$$s(x) = \sum_{i=1}^N \lambda_i \phi(\|x - x_i\|_2; \varepsilon) \text{ subject to } s(x_i) = f(x_i), \quad i = 1, \dots, N \quad (1)$$

¹Assuming positive definiteness of the RBF, as in definition 2.1

where λ_i are unknown coefficients, x_i are the interpolation nodes, ϕ is a radial function and ε is the *shape parameter* of ϕ , which governs the shape of the RBF and plays an important role on the accuracy of the approximation (e.g. for multiquadric basis functions [2]).

We can write (1) as a system of equations

$$\underline{\underline{A}}(\underline{x}, \varepsilon)\underline{\lambda} = \underline{f}(\underline{x}) \quad (2)$$

where $\underline{\underline{A}}(\underline{x}, \varepsilon) \in \mathbb{R}^{N \times N}$ is the interpolation matrix with entries $a_{ij} = \phi(\|x_i - x_j\|, \varepsilon)$, \underline{x} denotes a set of interpolation points $(x_1, \dots, x_N)^2$ and $\underline{f}(\underline{x}) = (f(x_1), \dots, f(x_N))$ is the unknown function evaluated at the interpolation nodes.

Table 1: Common positive definite radial basis functions.

Type of basis function	$\phi(r)$
Gaussian	$e^{-(\varepsilon r)^2}$
Inverse multiquadric	$(1 + (\varepsilon r)^2)^{-\beta/2}, \beta \geq 0$
Matérn	$K_\nu(\varepsilon r)(\varepsilon r)^\nu, \nu > 0$

Some examples of commonly used RBFs can be found in Table 1, all of which contain a *shape parameter* ε in their definition. How to correctly choose the shape parameter on a RBF has been a topic of much study; it can be treated as a hyper-parameter that is problem dependent, fixed by trial and error. Another approach is to consider an adaptive strategy that depends on the configuration of the interpolation nodes and on the function values at the interpolation nodes. An early contribution was by Hardy [3], where he suggested an adaptive shape parameter given by

$$\varepsilon = 1/(0.815d), \quad \text{with } d = (1/N) \sum_{i=1}^N d_i, \quad (3)$$

where N is the total number of interpolation nodes and d_i is the distance between the i -th data point and its nearest neighbour. Franke [4] replaced d by D/\sqrt{N} where D is the diameter of the minimal circle enclosing all data points and suggested to compute the shape parameter as

$$\varepsilon = 0.8\sqrt{N}/D. \quad (4)$$

Later, the modified Franke method modified the square-root to read $\varepsilon = 0.8\sqrt[4]{N}/D$ [5]. Foley [6] used a similar value for the shape parameter based on the area of the bounding rectangle to the data. These proposed methods take into consideration the placement of the interpolation nodes $\{x_i\}_{i=1}^N$ but ignore the function values $\{f(x_i)\}_{i=1}^N$.

Foley and Carlson proposed a method by examining statistical properties such as the root-mean-square (RMS) error, taking into account not only the nodal placement but also function values [2]. Other methods focusing on reducing the RMS have been proposed [7, 8]. Another method that has become very popular is by using cross-validation. The leave-one-out cross

²Throughout the paper, we use an abuse of notation to denote both the set of points $\{x_1, \dots, x_N\}$ and the ordered vector (x_1, \dots, x_N) with \underline{x} , as the corresponding object is usually clear.

validation (LOOCV) method selects the shape parameter ε by minimising the norm of an error vector $\underline{E}(\varepsilon) = (E_1(\varepsilon), \dots, E_N(\varepsilon))$:

$$\arg \min_{\varepsilon} \| (E_1(\varepsilon), \dots, E_N(\varepsilon)) \|, \quad \text{where } E_k(\varepsilon) = f(x_k) - s^{(k)}(x_k, \varepsilon) \quad (5)$$

with $s^{(k)}$ being the interpolant to a reduced data set, obtained by removing the node x_k and the corresponding function value $f(x_k)$. In [9], the LOOCV strategy is adopted to choose the shape parameter for multiquadric basis in the context of approximating PDEs. Later, Rippa [8] proposed another algorithm based on LOOCV, which does not require the computation of N distinct interpolants $s^{(k)}$, $k = 1, \dots, N$ but rather computes each entry in the error vector through:

$$E_k = \underline{\underline{A}}^{-1}(\underline{x}, \varepsilon) \underline{f} / \text{diag}(\underline{\underline{A}}^{-1}(\underline{x}, \varepsilon)), \quad k = 1, \dots, N \quad (6)$$

This idea has led to several extensions, for example: [10] the method of maximum likelihood estimation (MLE) is employed as an extension of the LOOCV-algorithm; another extension of Rippa’s algorithm presented is in [11] to work in a more general k -fold CV setting and in a stochastic setting [12].

In RBF, a key challenge is solving the problem without encountering the Runge phenomenon. In [13] determined the shape parameter with consideration for the limitations of the Runge phenomenon. They suggested that instead of using a constant parameter, the data should be clustered and a separate shape parameter calculated for each cluster. Other efforts in spatially variable shape parameters in RBF have been explored [7, 14], as they offer adaptability to local variations, enabling dynamic adjustments to capture intricate spatial features.

In [15, 16] the RBF Contour Padé (RBF-CP) method is introduced; it first computes the solution at various values of the shape parameter along a secure path in the complex plane, and then the solution is approximated at the desired positive shape parameter using Padé approximation.

In a recent study, we presented a methodology for training a neural network (NN) in an unsupervised fashion to predict an optimal shape parameter for Gaussian and Inverse Multiquadric RBFs[17]. Although we demonstrated that this proposed methodology was robust across various tasks, it required a specific structure on the cloud points for $n = 2$. In this work, we present a natural continuation of that work by making the following contributions:

- We formulate an easy to solve optimisation problem to find the shape parameter ε for any set of points $\underline{x} \subset \mathbb{R}^n$ of size N while controlling the condition of the interpolation matrix $\underline{\underline{A}}$ (Section 3);
- Using the optimisation problem, we create a dataset that is used to train a NN to predict the shape parameter ε given any set of points $\underline{x} \subset \mathbb{R}^n$ of size N (Sections 4.1 and 4.2);
- We provide a fallback procedure that guarantees that the proposed shape parameter generates a well-posed interpolation matrix (Section 4.3).

In this work, we do not need to explicitly treat the 1–dimensional and 2–dimensional cases differently, instead, we consider the distances between the nodes, thus the task depends on the number of interpolation points N .

The paper is structured in the following way: in Section 2 we provide a summary of results about RBFs, in Section 3 we describe the 1–dimensional optimisation problem with respect to ε that bounds the condition of the interpolation matrix, then, in Sections 4.1 and 4.2 we describe the dataset and data-driven method to predict the shape parameter ε and in Section 4.3 we present the fallback procedure. In Section 5 we present some numerical experiments and test the performance of our proposed model. Lastly, in Section 6 we finish with some conclusions and future work.

2 Radial basis functions

In this work, we assume positive definite RBFs.

Definition 2.1. A RBF ϕ on $[0, \infty)$ is **positive definite** on $\Omega \subset \mathbb{R}^n$, if for all choices of sets $\underline{x} := \{x_1, \dots, x_N\}$ of finitely many points $x_1, \dots, x_N \in \mathbb{R}^n$ and arbitrary $N \in \mathbb{N}$, the symmetric $N \times N$ matrix \underline{A} with entries $\underline{A}_{ij} = \phi(\|x_i - x_j\|, \varepsilon)$ is positive definite.

This is a standard assumption and many commonly used RBFs have this property (e.g. Table 1).

The RBF method for the interpolation of scattered data is given as in (1). The RBF basis can be augmented by polynomials of a certain maximal degree, leading to the following augmented form of s :

$$s(x) = \sum_{i=1}^N \lambda_i \phi(\|x - x_i\|, \varepsilon) + \sum_{k=1}^m \gamma_k p_k(x), \quad (7)$$

with $m = \binom{D_m + (n-1)}{n-1}$, where D_m is the degree of the monomial basis, γ_k is a linear coefficient and p_k a basis for the space of polynomials up to degree $D_m - 1$, denoted by \mathcal{P}_{D_m-1} . The RBF interpolant (7) of a function f is uniquely determined by the conditions:

$$\begin{aligned} s(x_i) &= f(x_i), \quad i = 1, \dots, N \\ \sum_{i=1}^N \lambda_i p_\ell(x_i) &= 0, \quad \ell = 1, \dots, m \end{aligned} \quad (8)$$

The addition of polynomials in the approximation space can be beneficial for several reasons:

- Some RBFs (e.g. the thin-plate spline) are conditionally positive definite, i.e. they only attain a positive definite interpolation matrix in the subspace that satisfies (8),
- Their inclusion leads to a better representation of the constant function and low order polynomials and to a better general accuracy of the approximation [18].

2.1 Solving partial differential equations

We consider the radial basis function based finite difference (RBF-FD) method for solving steady-state and time dependent differential equations. This is a meshfree method to solve PDEs numerically, generated from RBF interpolation over local sets of nodes on the surface [19, 20], meaning that only a nearest neighbour region is connected to each basis function.

Then, we have a cluster of point clouds where the cardinal basis are considered locally inside the cloud, leading to a sparse matrix instead of a dense linear system of equations.

In this section, we derive the RBF-FD formulation [21] for the Poisson equation and time dependent differential equations. We are interested in the solution of PDEs of the following forms:

$$\Delta u(x) = f(x) \quad \text{or} \quad \mathcal{L}u(x) = f(x), \quad x \in \Omega, \quad (9)$$

where Δ is the Laplace operator and \mathcal{L} denotes the space differential operator which can be also used in a more general setting. Equation (9) is complemented by boundary conditions. The domain Ω is discretized using two sets of points:

- The interpolation node set $X = \{x_i\}_{i=1}^M$ for generating the cardinal functions.
- The evaluation node set $Y = \{y_j\}_{j=1}^P$ for sampling the PDE (9).

The difference between the two sets is that X is used to build the underlying approximation space whereas at the nodes Y , the PDE is actually solved. When $X = Y$, this corresponds to a collocation method and when $M > N$, it is referred as oversampling. The cardinality of the X and Y node sets matches the relation $P = rM$, where r is the oversampling parameter.

We consider first the time independent problem for simplicity. Using the interpolation node set X , we form a stencil for each $x_i \in X$, based on the N nearest neighbors. Each stencil (also referred as node's support domain) is represented with a node set $\underline{x}_i = \{x_1^{(i)}, \dots, x_N^{(i)}\}$, $i = 1, \dots, M$. We consider the standard RBF interpolant using inverse multiquadric function with a constant polynomial so that the RBF-FD formula is exact for constants, as in (7) with $m = 1$, imposing the conditions (8). This leads to a symmetric, block linear system of equations:

$$\underbrace{\begin{bmatrix} \underline{\Phi} & \underline{\mathbb{1}} \\ \underline{\mathbb{1}} & \underline{0} \end{bmatrix}}_{\underline{A}} \underbrace{\begin{bmatrix} \underline{\lambda} \\ \underline{\gamma} \end{bmatrix}}_{\underline{c}} = \underbrace{\begin{bmatrix} \underline{u} \\ \underline{0} \end{bmatrix}}_{\underline{u}_{aug}}, \quad (10)$$

where $\underline{\Phi}_{k\ell} = \phi(\|x_k - x_\ell\|)$, $k, \ell = 1, \dots, N$. On each stencil node set \underline{x}_i , we form a local interpolation problem leading to a set of stencil based approximations given by

$$u^{(i)}(y) = [\underline{\Phi}(y) \quad \underline{\mathbb{1}}] \underline{c} = [\underline{\Phi}(y) \quad \underline{\mathbb{1}}] \underline{A}^{-1} \underline{u}_{aug} = \sum_{j=1}^N u(x_j^{(i)}) \psi_j^{(i)}(y), \quad \forall i = 1, \dots, M \quad (11)$$

where $\psi_j^{(i)}(y)$ are the local RBF-FD cardinal functions with Kronecker delta property ($\psi_j^{(i)}(z) = 1$ if $z = x_j$, 0 otherwise) and $u^{(i)}(y)$ is the local approximation (see more details of the method's derivation in [22]).

To obtain a global solution at any y , we associate every evaluation node with an index of the closest stencil center node defined by

$$\nu(y) = \arg \min_{i \in \{1, \dots, M\}} \|y - x_i\|.$$

Then, for every $y \in Y$, we can express the local solution as:

$$u^{\nu(y)}(y) = \sum_{j=1}^N \psi_j^{\nu(y)}(y) u(x_j^{\nu(y)}), \quad (12)$$

To get a global representation of the solution, we introduce an auxiliary index transformation $\sigma(j, \nu(y)) : \{1, \dots, N\} \times \{1, \dots, M\} \rightarrow \{1, \dots, M\}$ that maps from the j -th local weight of a stencil with index $\nu(y)$ to its global equivalent and rewrite (12):

$$u(y) = \sum_{i=1}^M u(x_i) \Psi_i(y) = \sum_{i=1}^M u(x_i) \sum_{j=1}^N \psi_j^{\nu(y)} \delta_{i, \sigma(j, \nu(y))}, \quad (13)$$

where Ψ_i are the global RBF-FD cardinal functions and $\delta_{i, \sigma(j, \nu(y))}$ selects the corresponding local ψ_j to be multiplied with the global nodal solution $u(x_i)$. It follows, in a similar fashion, that

$$\mathcal{L}u(y) = \sum_{i=1}^M u(x_i) \mathcal{L}\Psi_i(y) = \sum_{i=1}^M u(x_i) \sum_{j=1}^N \mathcal{L}\psi_j^{\nu(y)} \delta_{i, \sigma(j, \nu(y))}, \quad (14)$$

which is used in the discretization. This means in the steady-state case, we solve the system of equations on the evaluation points using the following discretization:

$$\sum_{i=1}^M u(x_i) \mathcal{L}\Psi_i(y_j) = f(y_j), \quad \forall j = 1, \dots, P.$$

Let us now consider the initial-boundary value problem

$$\frac{\partial u(x, t)}{\partial t} = \mathcal{L}u(x, t), \quad x \in \Omega, \quad 0 \leq t \leq T, \quad (15)$$

$$u(x, t) = g(x, t), \quad x \in \partial\Omega, \quad (16)$$

$$u(x, 0) = f(x), \quad x \in \Omega. \quad (17)$$

where $\Omega \subset \mathbb{R}^n$ is the solution domain with the boundary $\partial\Omega$ where Dirichlet boundary conditions are considered and \mathcal{L} is a differential operator on \mathbb{R} .

The difference from before is the dependence of u in space and time now. By using a simple method of lines (MOL) approach, we split the space and time discretization in the usual way. For the space discretization the RBF-FD discretization is applied, where now the coefficients depend in time and are updated via classical time-integration schemes like Runge-Kutta (RK) methods, backward differentiation formulas (BDFs) or deferred correction schemes (DeC). Analogous to (14), we have now

$$\mathcal{L}u(y, t) = \mathcal{L}u^{\nu(y)}(y, t) = \sum_{i=1}^M u(x_i, t) \mathcal{L}\Psi_i(y) \quad (18)$$

and we obtain a linear system of ordinary differential equations from (15) that involve the time dependent coefficients $u(x_i, t)$.

In this work we consider (9) or (15) with Dirichlet boundary conditions. When computing the numerical solution in time, we use the injection method to impose the condition, i.e., we overwrite the solution $u(x, t_k)$, $k = 0, 1, \dots$ with the corresponding boundary value, after each step of the time-stepping algorithm.

2.2 Error and stability

By definition 2.1, we can define a positive definite kernel

$$\Phi : \Omega \times \Omega \rightarrow \mathbb{R}, \quad \Phi(x, x') = \phi(\|x - x'\|),$$

which is a symmetric real-valued function of two variables. Let us define the function space

$$H_\Phi(\Omega) = \text{span}\{\Phi(\cdot, x) : x \in \Omega\},$$

and the associated bilinear form

$$\left\langle \sum_{i=1}^N c_i \Phi(\cdot, x_i), \sum_{k=1}^N d_k \Phi(\cdot, x_k) \right\rangle_\Phi = \sum_{i=1}^N \sum_{k=1}^N c_i d_k \Phi(x_i, x_k),$$

which defines an inner product on $H_\Phi(\Omega)$. By Moore-Aronszajn's theorem, there exists a unique Reproducing Kernel Hilbert space (see details of construction in Chapter 10, [1]) associated to Φ , the so-called *native space* \mathcal{N}_Φ with norm induced by $\langle \cdot, \cdot \rangle_\Phi$, expressed as $\|\cdot\|_{\mathcal{N}_\Phi}$. The pointwise error estimate for any point $x \in \Omega$ between an interpolator defined over interpolation nodes $\underline{x} = x_1, \dots, x_N$ and $f \in \mathcal{N}_\Phi$ can be expressed as[1]:

$$|f(x) - s_{f, \underline{x}}(x)| \leq P_{\Phi, \underline{x}} \|f\|_{\mathcal{N}_\Phi}.$$

The interpolation error can be estimated through two independent quantities:

- the smoothness of the data, which is measured in terms of the native space norm of f , which is independent of the position of the interpolation nodes
- the contribution due to the use of the basis function Φ and the distribution of the data, measured in terms of the so-called *power function* $P_{\Phi, \underline{x}}$, which is independent of the data values.

It has been observed numerically and studied theoretically there exists a link between the approximation error and the condition of the interpolation matrix (measured by the smallest eigenvalue of $\underline{A}(\underline{x}, \varepsilon)$)[23]. It is known as the *trade-off principle* (or also Uncertainty principle) in RBF interpolation, that states that “*there is no case known where the error $P_{\Phi, \underline{x}}$ and the sensitivity λ_{\min}^{-1} are both reasonably small*”.

For example, considering the Gaussian or inverse multiquadric basis, if one keeps the number of interpolation nodes fixed and increases the value of ε , then the condition number of \underline{A} is improved but the accuracy of the interpolant deteriorates. Conversely, one can attempt to improve the accuracy of a RBF interpolant by decreasing ε . However, this is only possible at the cost of numerical instability (ill-conditioning of A)[24].

In this part, we present some existing results on the asymptotic behaviour of the interpolation matrix $\underline{A}(\underline{x}, \varepsilon)$ as $\varepsilon \rightarrow 0$ or $\varepsilon \rightarrow \infty$. We focus on the inverse multiquadric or Gaussian functions, with the inverse relation for multiquadric function.

Proposition 1. For any collection of distinct points $\underline{x} \in \mathbb{R}^{N \times n}$:

$$\lim_{\varepsilon \rightarrow \infty} A(\underline{x}, \varepsilon) = \mathcal{I}_n$$

$$\lim_{\varepsilon \rightarrow 0} A(\underline{x}, \varepsilon) = \underline{1}_n$$

Proof. We note the structure of $A(\underline{x}, \varepsilon) = \mathcal{I}_n + Q$, where each entry of $Q_{ij} = \phi(r_{ij}; \varepsilon)$ and zero diagonal. As $\varepsilon \rightarrow 0$, $\phi(r_{ij}; \varepsilon) = 1$ for $i \neq j$. Similarly, as $\varepsilon \rightarrow \infty$, $\phi(r_{ij}, \varepsilon) = 0$ for $i \neq j$. ■

Proposition 2. For any collection of distinct points $\underline{x} \in \mathbb{R}^{N \times n}$, the eigenvalues of $A(\underline{x}, \varepsilon)$ converge to 1 as $\varepsilon \rightarrow \infty$.

Proof. Let $D(a, r)$ denote the disk with center a and radius r on the complex plane:

$$D(a, r) = \{x \in \mathbb{C} : |x - a| \leq r\}.$$

For $A \in \mathbb{R}^{N \times N}$, the Gerschgorin circles are defined as $D(1, R_i)$ where $R_i = \sum_{j:i \neq j} |m_{ij}|$. By the Gerschgorin circle theorem, every eigenvalue of A lies in some $D(m_{ii}, R_i)$.

Namely, $R_i = \sum_{j:j \neq i} \phi(r_{ij}, \varepsilon) \rightarrow 0$ as $\varepsilon \rightarrow \infty$, so the eigenvalues lie inside the disc with a shrinking radius centered at 1. ■

The other asymptotic regime, $\varepsilon \rightarrow 0$, is of special interest due to the connection to Lagrange polynomial interpolation, as shown initially in [25] for the uni-variate case, and subsequently for the multivariate cases. This is called the *flat-limit* regime, which assumes that the set of nodes \underline{x} is arbitrary but fixed. In [26], formulas are derived for the determinant and eigenvalues of the interpolation matrix for small ε that show the monotonicity of the eigenvalues for kernels with different smoothness and in the uni-variate and multivariate cases. For example, in the uni-variate case for the Gaussian kernel, they show that the eigenvalues $\lambda_k(\varepsilon)$ are of order $\mathcal{O}(\varepsilon^{2(k-1)})$ (Theorem 4.2).

3 Controlling the interpolation matrix condition

In this section, we describe a procedure to find a shape parameter ε for any given set of N points $\underline{x} \subset \Omega \subset \mathbb{R}^n$ that maintains the condition number of the interpolation matrix inside a specified range.

Consider the logarithm (in base 10) of the condition number of the interpolation matrix:

$$\text{logcond}(\underline{x}, \varepsilon) := \log_{10} (\text{cond}_F(\underline{A}(\underline{x}, \varepsilon))),$$

where

$$\text{cond}_F(\underline{x}, \varepsilon) = \|\underline{A}(\underline{x}, \varepsilon)\|_F \|\underline{A}(\underline{x}, \varepsilon)^{-1}\|_F$$

computed with respect to the Frobenius norm:

$$\|\underline{A}(\underline{x}, \varepsilon)\|_F = \sqrt{\sum_{i=1}^N \sum_{j=1}^N |a_{ij}|^2}.$$

Let us consider the following minimisation problem:

$$\varepsilon^* = \arg \min_{\varepsilon \in \mathbb{R}^+} \ell(\text{logcond}(\underline{x}, \varepsilon)), \tag{19}$$

where ℓ is a simple piecewise linear convex loss:

$$\ell(x) = \begin{cases} x - b & x > b \\ 0 & b \geq x \geq a \\ -x + a & x < a \end{cases}. \tag{20}$$

for some $a, b \in \mathbb{R}$. A zero loss is attained when the logarithm (in base 10) of the matrix condition is between the range $[a, b]$. This range is chosen as a balance between double precision and interpolation error, but can be changed according to numerical accuracy requirements, for example. In the numerical experiments shown throughout the paper, we set $a = 11, b = 11.5$ unless otherwise specified. We adopt a gradient descent optimisation strategy to solve (19). The minimisation problem above can provide an ϵ for points with any dimension. Some examples of the results of this optimisation procedure compared with other adaptive strategies is shown in Figure 1 for sets of arbitrary nodes in 1-dimension and varying the interval where the interpolation nodes are.

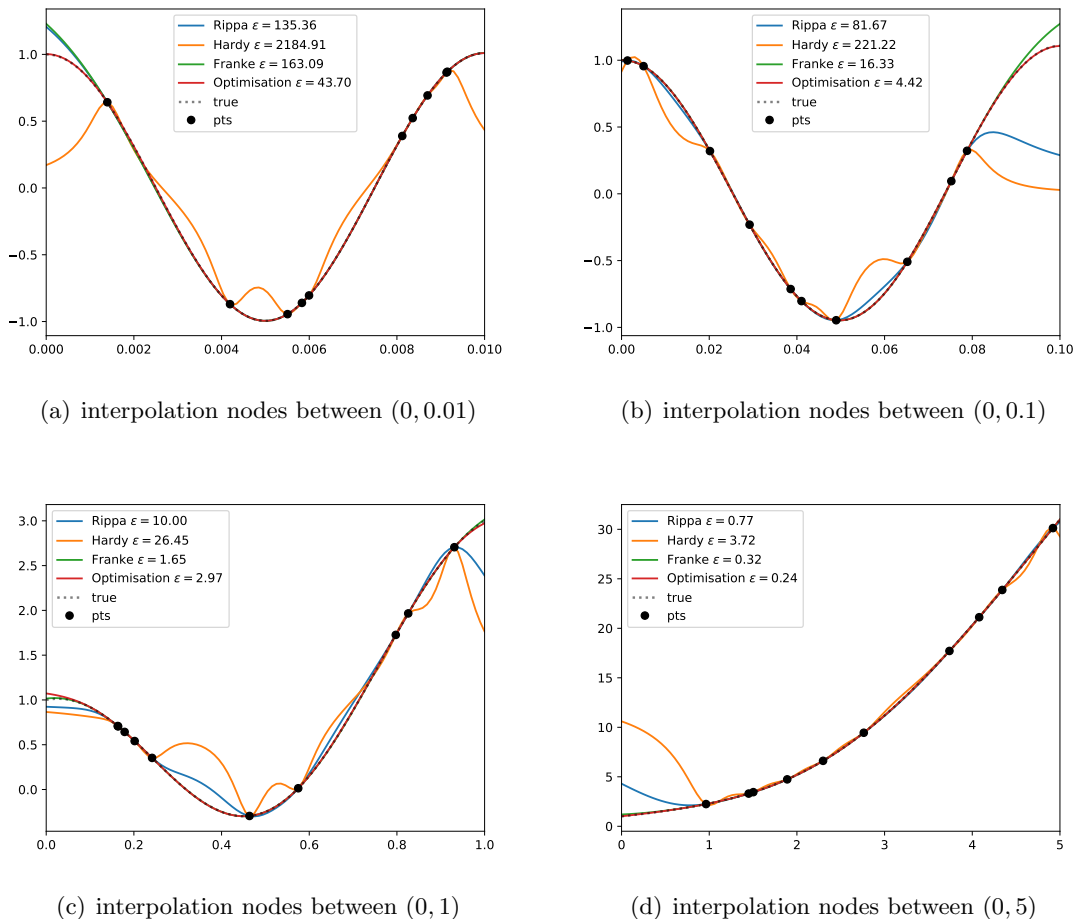


Figure 1: Visual comparison between different adaptive methods and the optimisation method presented above on the 1–dimensional function $f(x) = \cos(2/b\pi x) + x^2 + x$, where b is the maximum range of the interval.

To study the convergence to a critical point when using gradient descent type optimisation, we study the objective function defined above, which is given by:

$$\mathcal{L}(\epsilon) = \ell \circ \log_{10} \circ \text{cond} \left(\underline{\underline{A}}(x, \epsilon) \right).$$

It is a function composition of a convex function ℓ , a monotonically increasing function \log_{10} and cond . Thus if $\text{cond}(\underline{A}(\underline{x}, \cdot))$ is strictly monotonically decreasing with respect to ε , then the function composition above preserves the convexity of ℓ and gradient descent converges.

We investigate numerically the derivative $d_\varepsilon \text{cond}$:

$$d_\varepsilon \text{cond}(\underline{x}, \varepsilon) = \frac{\|\underline{A}(\underline{x}, \varepsilon)^{-1}\|_F \text{Tr}(\underline{A}(\underline{x}, \varepsilon) \underline{A}'(\underline{x}, \varepsilon))}{\|\underline{A}(\underline{x}, \varepsilon)\|_F} + \frac{\|\underline{A}(\underline{x}, \varepsilon)\|_F \text{Tr}(-\underline{A}'(\underline{x}, \varepsilon) [\underline{A}^{-1}(\underline{x}, \varepsilon)]^3)}{\|\underline{A}(\underline{x}, \varepsilon)^{-1}\|_F}, \quad (21)$$

where $\underline{A}'(\underline{x}, \varepsilon)$ is the derivative of the matrix $\underline{A}(\underline{x}, \varepsilon)$ with respect to ε . In Figure 2, we show the derivative value (under the transformation $\exp(\cdot)$ for visualisation convenience) for different selection of \underline{x} nodes in one and two dimensions, while varying ε . We observe that the sign of the derivative, far from $\varepsilon \rightarrow 0$ is always negative in our numerical investigations, pointing towards the condition number being strictly monotonically decreasing with respect to ε . We were, however, unable to rigorously prove the statement except for the simple case of $N = 2$ (through a direct computation of the Frobenius norm) and leave it as an open conjecture:

Conjecture 1. *For the Gaussian or Inverse Multiquadric RBF, let $\varepsilon_1 > \varepsilon_2$. For any set of distinct points $\underline{x} \subset \Omega \subset \mathbb{R}^n$, let $\underline{A}_1 = \underline{A}(\underline{x}, \varepsilon_1)$ and $\underline{A}_2 = \underline{A}(\underline{x}, \varepsilon_2)$. Then, $\text{cond}(\underline{A}_1) \leq \text{cond}(\underline{A}_2)$.*

In [26] it has been shown that when $\varepsilon \in [0, \varepsilon_0]$ for small positive ε_0 , the monotonicity condition is true for the spectral norm, as the smallest eigenvalue is of order $\mathcal{O}^{2(N-1)}$, whereas the largest eigenvalue is of order $\mathcal{O}(1)$ (when considering an infinitely smooth kernel and in the uni-variate case).

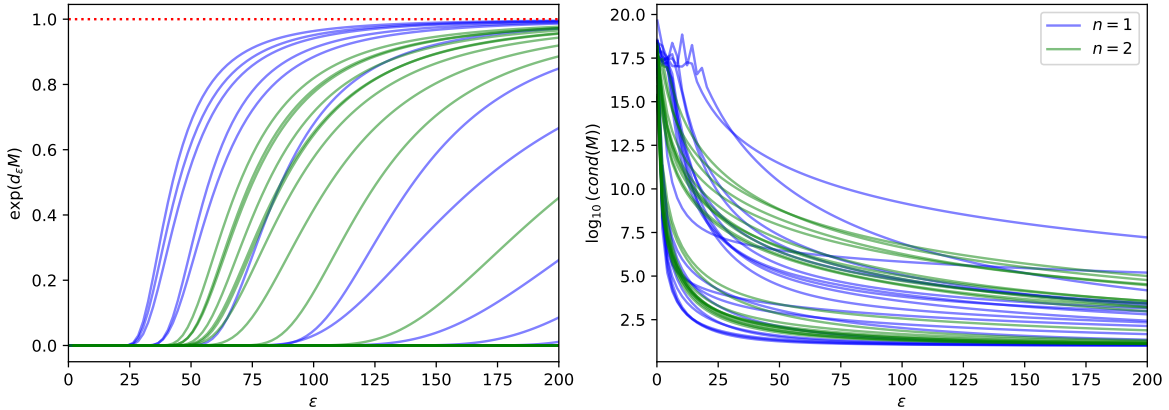


Figure 2: Left: Derivative of matrix condition as a function of ε for randomly generated sets of points in 1-dimension (blue) and 2-dimensions (green). Right: Logarithm of the interpolation matrix condition as a function of ε .

4 Learning model

4.1 Dataset generation

Given the optimisation problem (19) described in the previous section, we can obtain a suitable ε for a set of points \underline{x} . Then, we can generate a dataset for our learning problem. We consider clouds of points embedded in 1-dimension and 2-dimensions, generating in total 6300 training points in 1-dimension and 12000 training points in 2-dimensions. We vary the range of the domain, between $[0, 0.001]$ to $[0, 1]$ to guarantee a good coverage of lengthscales and we also use different interpolation functions to have a sense of the error of the method, although we did not use the interpolation error information for the dataset generation. More details can be found in Appendix A, where the datasets are summarised in Tables 5 and 6 and the algorithm used for generating dataset is depicted in Algorithm 2.

Remark 1. While the dimensionality of the interpolation nodes does not change the optimisation problem, as it depends on the distance matrix of the points, we still initially distinguished the 1-dimensional from the 2-dimensional setting to understand the learning problem.

Remark 2. The generation of the dataset labels can be replaced. For example, one could use the well-known LOOCV procedure to find optimal ε , at the cost of extra computation and dependency on the function values, which would make the method not agnostic to the function to be interpolated. In particular, this restriction can become relevant in the context of RBF-FD because the solution is not known *a priori* for all times.

4.2 Learning strategy

We want to find a mapping between a set of interpolation nodes $\underline{x} \subset \Omega \subset \mathbb{R}^n$ and an optimal shape parameter ε that satisfies accuracy and stability of the system. Therefore, we formulate the learning goal as follows: find a function f for which given a set of N arbitrary points, denoted by the set $\underline{x} \subset \mathbb{R}^n$ (which is represented as a matrix $\underline{x} \in \mathbb{R}^{N \times n}$), returns ε such that the condition number of the interpolation matrix $\underline{\underline{A}}(\underline{x}, \varepsilon)$, generated using RBFs with parameter ε and set of interpolation nodes \underline{x} , is within the specified matrix condition range.

$$f : \underline{x} \in \mathbb{R}^{N \times n} \rightarrow \varepsilon \quad \text{s.t.} \quad \log\text{cond}(\underline{\underline{A}}(\underline{x}, \varepsilon)) \in [a, b]. \quad (22)$$

We use the technique in the Section 4.1 to generate the 1-dimensional and 2-dimensional datasets. Given a set of points $\{x_i\}_{i=1}^N$, we define the distance matrix as follows:

$$D(\underline{x}) = \begin{bmatrix} \|x_1 - x_1\| & \|x_1 - x_2\| & \dots & \|x_1 - x_N\| \\ \|x_2 - x_1\| & \|x_2 - x_2\| & \dots & \|x_2 - x_N\| \\ \dots & \dots & \dots & \dots \\ \|x_N - x_1\| & \|x_N - x_2\| & \dots & \|x_N - x_N\| \end{bmatrix}. \quad (23)$$

The distance matrix does not change with the dimension of the points x_i , only with the number of points considered. Furthermore, because the distance matrix is symmetric with zero diagonal, we can consider the features to be given by the inverse of upper part³ of the matrix D , namely, we define the features to be given by $\underline{d} = (\frac{1}{d_{ij}})_{1 \leq i \leq N, i < j \leq N}$ yielding a

³Or lower part.

vector of dimension $N_{in} = N(N - 1)/2$. We also sort the cloud of points before generating the distance matrix.

We use a dense, fully connected NN to approximate the map in (22). We assume that the map f can be approximated by \mathcal{F} in the form

$$\mathcal{F}(\underline{d}) := \sigma_k(\dots\sigma_1(W_1\underline{d} + b_1)), \quad (24)$$

where \underline{d} is the input vector, $\{\sigma_i\}_{i=1}^k$ are the activation functions, $\{W_i\}_{i=1}^k$ are the matrices in $\mathbb{R}^{N_i \times N_{i-1}}$ and $\{b_i\}_{i=1}^k$ are vectors in \mathbb{R}^{N_i} . $\{W_i\}_{i=1}^k$ and $\{b_i\}_{i=1}^k$ are learnable parameters, represented generically as w . Note that N_0 is the input dimension (i.e. for our case, $N_0 = \frac{N(N-1)}{2}$) and N_k is the output dimension (i.e. for our case, $N_k = 1$). The architecture of \mathcal{F} is specified in table 2.

Table 2: Architecture of NN, assuming $N = 10$.

Layer	Input size	Output size	Activation
Layer 1	$N_0 = 45$	$N_1 = 64$	ReLU
Layer 2	$N_1 = 64$	$N_2 = 64$	ReLU
Layer 3	$N_2 = 64$	$N_3 = 64$	ReLU
Layer 4	$N_3 = 64$	$N_4 = 32$	ReLU
Layer 5	$N_4 = 32$	$N_5 = 16$	ReLU
Layer 6	$N_5 = 16$	$N_6 = 1$	Linear

We consider the training paradigm known as supervised learning, in which the desired output value for the points in the training set are known in advance. The goal of the training is to minimize the error between the predictions and the actual values. We use a simple mean squared loss as the loss function:

$$\mathcal{L}(w) = \frac{1}{M} \sum_{i=1}^M (\varepsilon_i - \mathcal{F}(\underline{d}_i; w))^2,$$

where w denotes the learnable parameters and \underline{d}_i denotes the feature generated from points \underline{x}_i , over a dataset of size M . The loss function is augmented with a L_2 regularisation of the networks weights with parameter $\alpha = 0.00005$, which is a standard way to prevent over-fitting of the training data. The loss is minimized using the Adam optimizer, with parameters $\beta_0 = 0.9$, $\beta_1 = 0.999$ and learning rate $\eta = 10^{-5}$.

Remark 3. Other architectures to approximate the map in (22) have been considered, such as Convolutional Neural Networks and Encoder-Decoder networks but there was no significant benefit to using more complicated architectures, so we omit those results from this work. We also considered the full distance matrix (23) as our features, and that lead to worse results.

4.3 Performance estimation and fallback procedure

To have an estimate of the performance of the network’s output $\hat{\varepsilon}$, we can evaluate the condition of the interpolation matrix $\underline{\underline{A}}(\underline{x}, \hat{\varepsilon})$ and verify if it is below a certain acceptable

threshold θ . If the condition of the generated interpolation matrix has a condition larger than the acceptable threshold θ , we correct the shape parameter by calling the optimisation procedure defined in Section 3 and replacing the predicted $\hat{\varepsilon}$. The full algorithm is shown in algorithm 1.

Remark 4. Other performance indicators could be used. For example, in the case of pure interpolation, the LOOCV error E can be considered, and if it is above a user defined threshold, the LOOCV procedure can be used to replace the predicted $\hat{\varepsilon}$. This was not explored in this work and we leave it to future work.

Algorithm 1: Shape prediction with fall-back

Input: Set of interpolation notes $\underline{x} \in \mathbb{R}^{N \times n}$, threshold θ

Output: ε

$\underline{d} \leftarrow$ generate features from \underline{x}

$\varepsilon \leftarrow \mathcal{F}(\underline{d})$

if $\text{cond}(A(\underline{x}, \varepsilon)) > \theta$ **then**

 | $\varepsilon \leftarrow$ solve minimisation as in (19)

end

5 Numerical experiments

In this section, we test the shape parameter selection method, first evaluating the performance of our proposed method in interpolation tasks; then, in a finite-difference RBF (FD-RBF) method. We compare our proposed method to other well-known adaptive shape parameter methods such as Hardy [3], Franke [4], modified Franke, and Rippa’s LOOCV method [8].

Lastly, we evaluate our approach with the performance indicator, which is a hybrid approach that combines the NN’s prediction and the optimisation problem defined in Section 3, to guarantee that the proposed method remains robust.

In the following experiments, we consider the inverse multiquadric kernel and $N = 10$ points to build the interpolation, following the results of [17].

Some details on the training of the NN follow: we train one NN for both 1–dimensional and 2–dimensional test cases and we use an early stopping criteria, by setting the patience to $M = 200$. The network is trained using mini-batches of size 64. Figure 3 shows the plots of training loss and validation loss.

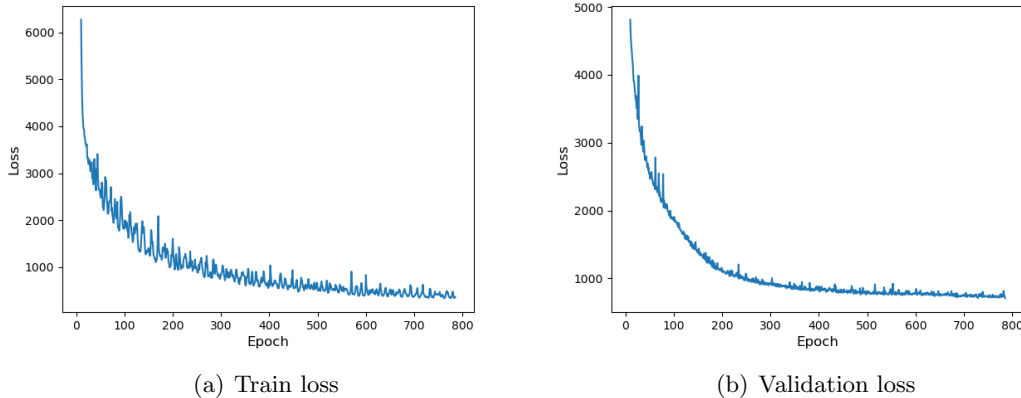


Figure 3: Training and validation losses during training.

Once the network has been trained, we use the same network for all the results shown in this section. We report the L_2 -error between the approximation via interpolation using a given shape parameter ε and the exact solution:

$$L_2\text{-error}(u_e, u_a) = \sqrt{\frac{1}{Q} \sum_{i=1}^Q |u_e(\tilde{x}_i) - u_a(\tilde{x}_i)|^2},$$

where u_e and u_a are the exact and approximate solutions and Q is the number of evaluation points \tilde{x} considered.

In our previous work, we showed a clear advantage of the variable shape parameter strategy using adaptive NN with respect to the constant shape parameter strategy [17]. Also, we observed that the error eventually blow-up in most the cases for constant shape parameter strategy. Hence, we only compare the proposed method with the Hardy, Franke, modified Franke and Rippa strategies, which are all adaptive methods. The comparison with the Rippa approach will only be done for interpolation tasks, where the function to be interpolated is known *a priori*, as this is a necessity for the Rippa approach.

The code developed to generate the datasets as well as the generated datasets, the set up of of the neural network and to the numerical experiments are in the github repository [27].

5.1 1D test cases

In this section, we perform numerical tests in one dimension for function interpolation (Section 5.1.1) and we solve a time-dependent PDE problem (Section 5.1.2).

For all the 1D tasks, the domain is discretized using both equidistant and non-equidistant centers, using the zeros of the Chebyshev polynomial of the first kind with degree $N = 10$ remapped to the interval $[0, 1]$. The refined mesh is created by adding midpoints. For interpolation task, we construct the interpolation using sets of N points, ensuring the boundary node overlaps between clusters.

5.1.1 Interpolation

We examine the performance of the proposed approach for the function f_1 , which is the combination of the exponential and trigonometric functions:

$$f_1(x) = e^{\sin(\pi x)} \quad x \in [0, 1]. \quad (25)$$

In Figure 4, we show the error convergence plot when using shape parameters obtained by our NN based approach and the adaptive methods Hardy, Franke, modified Franke and Rippa strategies, as a function of the number of centers for equidistant and non-equidistant points. Our strategy appears to yield a better approximation to interpolate function f_1 in most cases. For the Rippa method, we perform a search over the set of potential ε , given by \mathcal{E} as defined in (26), as implemented by the python package PySMO [28]. One can consider a larger grid to search over, at the expense of higher computational cost. Another observation was that as the interpolation nodes become closer, the interpolation matrix becomes numerically ill-conditioned for small ε , in such cases, we skip over that specific ε . Although Rippa can sometimes demonstrate a better performance, it requires the knowledge of f . Furthermore, because the proposed shape parameter ε_{Rippa} is restricted to the list (26), the list might not contain any element which is close enough to a good ε .

$$\mathcal{E} = [0.001, 0.002, 0.005, 0.0075, 0.01, 0.02, 0.05, 0.075, 0.1, 0.2, 0.5, 0.75, 1, 2, 5, 7.5, 10, 20.0, 50, 75, 100, 200, 500, 1000] \quad (26)$$

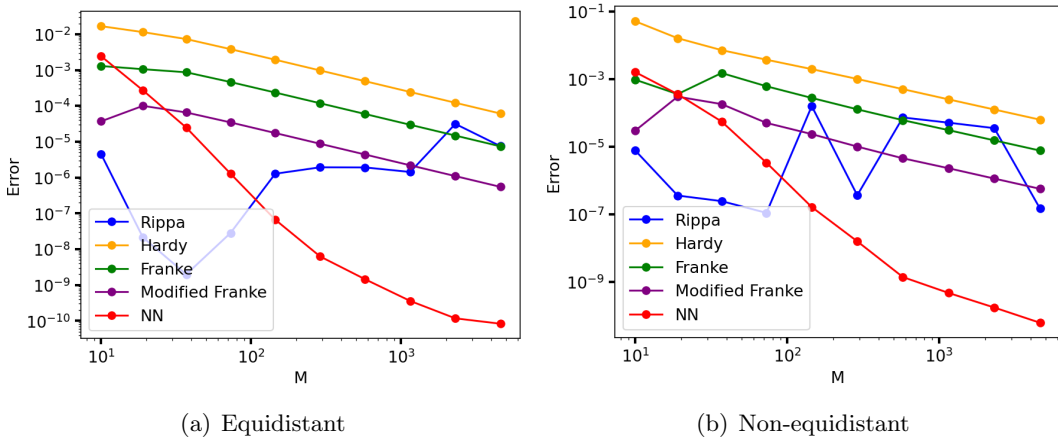


Figure 4: Error convergence plot for function f_1 .

We consider another test example, the well known Runge function:

$$f_2(x) = \frac{1}{1 + 16x^2}, \quad x \in [0, 1]. \quad (27)$$

Figure 5 shows the convergence plot using shape parameters obtained by the adaptive NN, Hardy, Franke, modified Franke and Rippa strategies, again as a function of the number

equidistant and non-equidistant points interpolation nodes. It can be easily seen that in both cases the adaptive NN is able to provide very good approximation for this task.

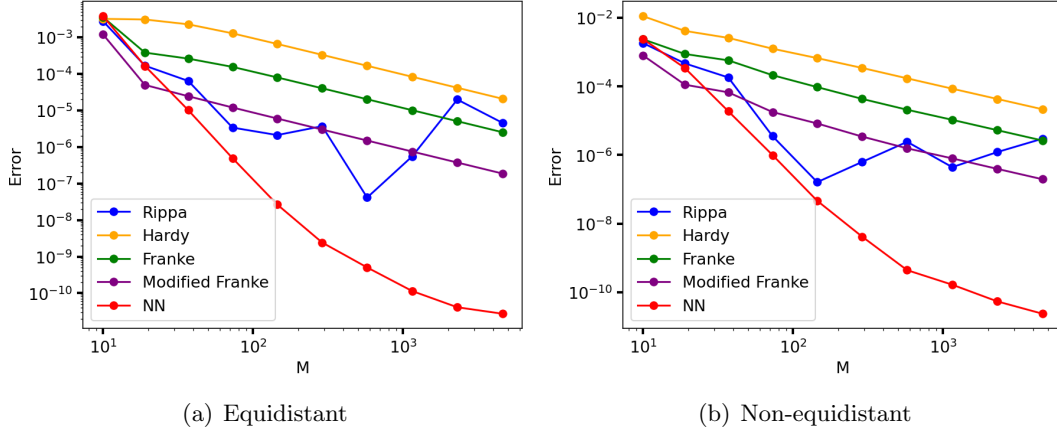


Figure 5: Error convergence plot for function f_2 .

Lastly, we consider a test example that consists of a piecewise constant problem:

$$f_3(x) = \begin{cases} 1, & \text{if } x > 0.5, \\ 0, & \text{if } x \leq 0.5, \end{cases} \quad x \in [0, 1]. \quad (28)$$

In Figure 6, we observe how all methods converge similarly, with the NN approach producing slightly lower errors. We also plot the resulting interpolation function for $N = 19$ and $N = 37$, comparing the adaptive NN, Hardy, Franke, modified Franke and Rippa strategies in Figure 7 and note that qualitatively, the interpolation does not look very different.

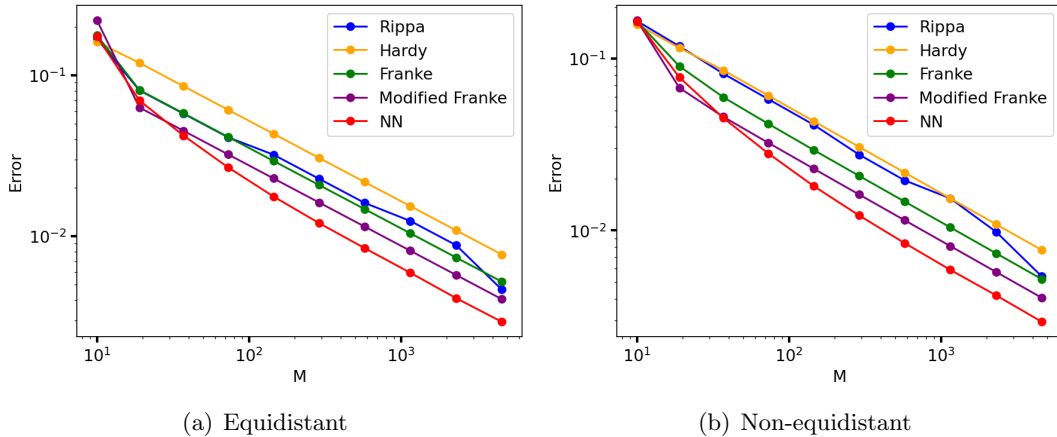


Figure 6: Error convergence plot for function f_3 .

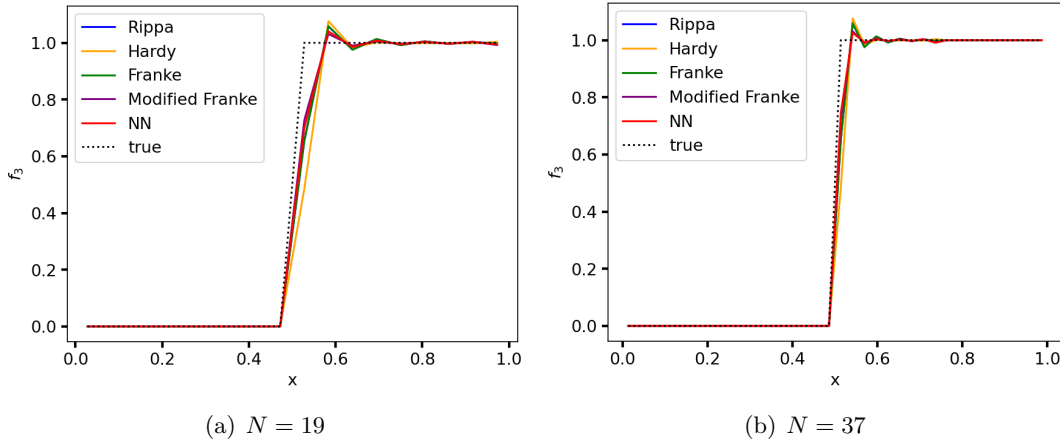


Figure 7: Comparison between numerical solution obtained with different strategies for f_3 for $N = 19$ and $N = 37$.

5.1.2 Time-dependent problem

In this section, we have tested our strategy on a 1D heat equation with two different initial conditions, and compared the RBF-FD method with the shape parameters obtained by the adaptive NN strategy with the RBF-FD method with shape parameters obtained with Hardy, Franke and modified Franke strategies. We consider the collocation method. We use BDF2 [29] for time stepping in all cases.

Consider the heat equation

$$\frac{\partial u}{\partial t} = \frac{\partial^2 u}{\partial x^2}, \quad x \in [0, 1], \quad 0 \leq t \leq T, \quad (29)$$

with the initial condition

$$u_1(x, 0) = -x^2 + x, \quad x \in (0, 1), \quad (30)$$

and the boundary conditions

$$u_1(0, t) = 0, \quad u_1(1, t) = 0, \quad 0 \leq t \leq T. \quad (31)$$

The exact solution of (29) with initial condition (30) and boundary conditions (31) is given by

$$u_1(x, t) = \sum_{n=1}^{\infty} \left(\frac{-4}{n^3 \pi^3} \right) ((-1)^n - 1) \sin(n\pi x) e^{-n^2 \pi^2 t}.$$

We set the time step to $\Delta t = 0.001$ and the final time to $T = 1$. The error between the analytical solution and the numerical solutions are shown in Figure 8(a) and Figure 8(b) for equidistant and non-equidistant interpolation nodes, respectively. We observe that our method has a superior performance. On the contrary, the errors do not decrease in the other strategies. Note that as M increases, the decay of the error is slower and it seems to stagnate. This might be due to the fact that we restrict the interpolation matrix condition to be bounded.

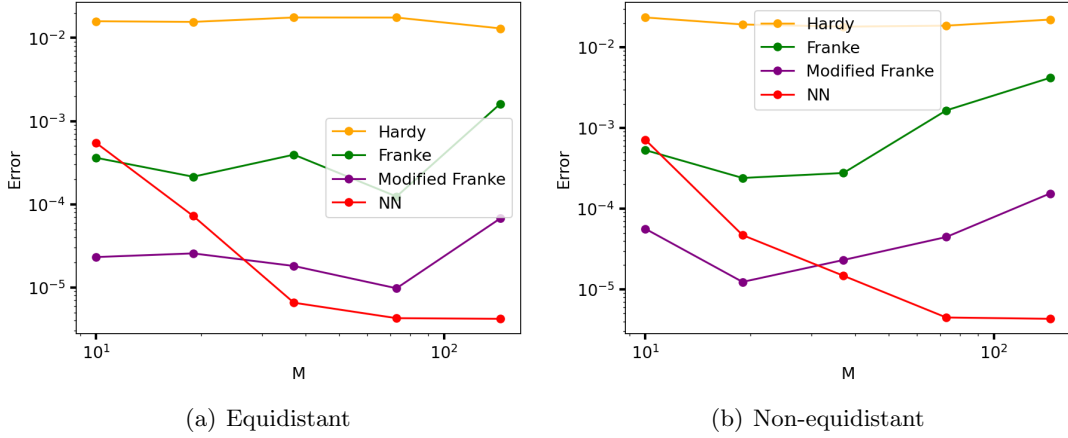


Figure 8: Convergence plot for the 1D heat problem with initial condition $u_1(x, 0) = -x^2 + x$.

We now consider again the heat equation (29) with another initial condition

$$u_2(x, 0) = 6 \sin(\pi x), \quad x \in (0, 1) \quad (32)$$

and the boundary conditions

$$u_2(0, t) = 0, \quad u_2(1, t) = 0, \quad 0 \leq t \leq 1. \quad (33)$$

The exact solution is given by

$$u_2(x, t) = 6 \sin(\pi x) e^{-\pi^2 t}.$$

In Figure 9(a) and Figure 9(b) the errors are shown for equidistant and non-equidistant points, respectively. It can be easily seen that only our approach converges to the exact solution. This figure shows that the other methods are unable to appropriately approximate the solution of (29).

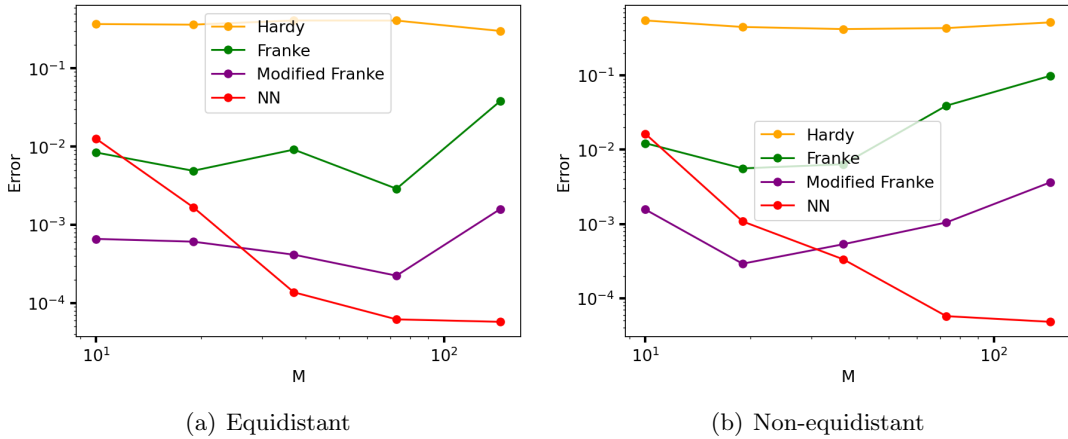


Figure 9: Convergence plot for the 1D heat problem with initial condition $u_2(x, 0) = 6 \sin(\pi x)$.

5.2 2D test cases

In this section, we present numerical experiments in two dimensions in the context of function interpolation (Section 5.2.1) and solving PDEs, namely, a boundary value problem (Section 5.2.2) and a time-dependent problem (Section 5.2.3). We generate the interpolation and evaluation point sets in two dimensions using regular Cartesian meshes to be able to observe error convergence. For interpolation problem, the oversampling parameter is set to 4 and for the other problems, we consider the collocation method.

5.2.1 Interpolation

We consider the well-known Franke function [24, 30]

$$f_4(x, y) = \frac{3}{4}e^{-\left(\frac{(9x-2)^2+(9y-2)^2}{4}\right)} + \frac{3}{4}e^{-\left(\frac{(9x+1)^2}{49} + \frac{(9y+1)^2}{10}\right)} + \frac{1}{2}e^{-\left(\frac{(9x-7)^2+(9y-3)^2}{4}\right)} - \frac{1}{5}e^{-\left((9x-4)^2+(9y-7)^2\right)}, \quad (x, y) \in [0, 1] \times [0, 1]$$

We show in Figure 10 the approximation error as we refine the mesh and note that the error in the adaptive NN approach is much smaller than for the other considered strategies. Rippa starts by performing well but as the number of interpolation points increases, the error does not diminish. This could be because the considered values listed in (26) are not sufficiently granular or the correct shape parameter does not belong in the covered interval.

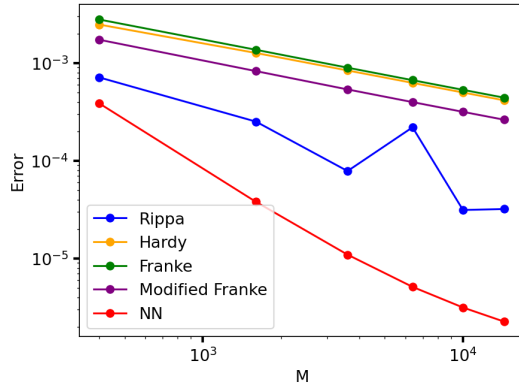


Figure 10: Error convergence plot for function f_4 .

Then, we consider the following function, that has been featured in previous works as the initial condition to a nonlinear PDE [30, 31, 32]:

$$f_5(x, y) = \left(1 + e^{-\frac{1}{\alpha}} - e^{-\frac{x}{\alpha}} - e^{-\frac{(x-1)}{\alpha}}\right) \left(1 + e^{-\frac{1}{\alpha}} - e^{-\frac{y}{\alpha}} - e^{-\frac{(y-1)}{\alpha}}\right), \quad (x, y) \in [0, 1] \times [0, 1]. \quad (34)$$

As α decreases, the problem becomes more difficult, as the function profile becomes more steep at the boundaries. In Figure 11, we plot the error convergence plot considering $\alpha = 0.1$ on the left and $\alpha = 1$ on the right. The advantages of using the novel method are evident: there is a significant difference in the errors between the adaptive NN and the other strategies. Note that the errors of the Hardy and of the Franke methods are essentially identical.

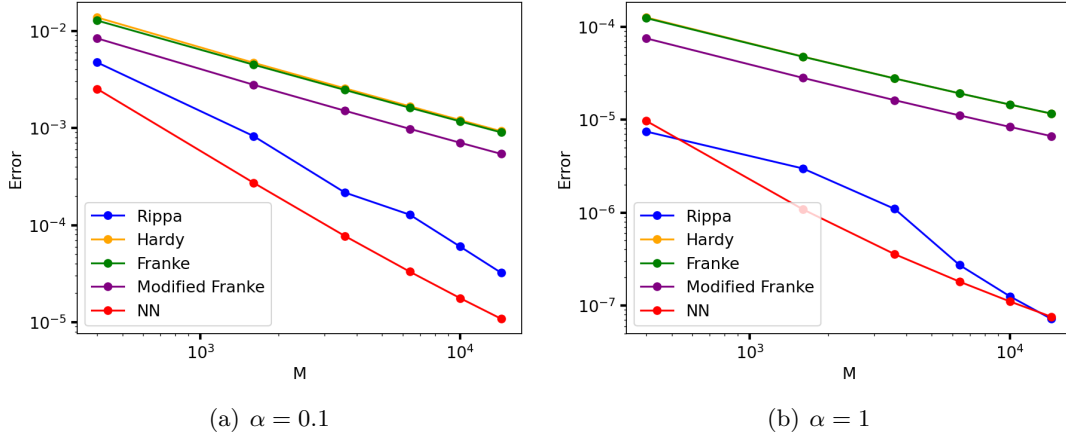


Figure 11: Error convergence plot for the function f_5 . $\alpha = 0.1$ on the left and $\alpha = 1$ on the right.

5.2.2 Boundary value problem

Let us consider the 2–dimensional linear elliptic boundary value problem

$$u_{xx} + u_{yy} = -4\pi^2 \sin(2\pi xy)(x^2 + y^2), \quad (x, y) \in [0, 1] \times [0, 1], \quad (35)$$

with boundary data

$$u(x, y) = \sin(2\pi xy), \quad (x, y) \in \partial([0, 1] \times [0, 1]). \quad (36)$$

The exact solution of (35) with boundary data (36) is $u(x, y) = \sin(2\pi xy)$. The error between the numerical solution and the analytical solution for this 2D linear elliptic boundary value problem is displayed in Figure 12. Again, we observe that the performance of the NN method superior to the performance of the other considered algorithms. In all other cases, the errors do not diminish (and some increase significantly) as the mesh is refined. We observe, however, that the NN method seems to stagnate in the finer meshes, and this can be due to the restriction on the matrix condition.

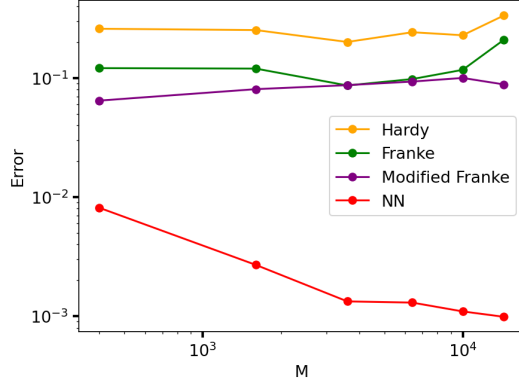


Figure 12: Convergence plot for Poisson equation with exact solution $u(x, y) = \sin(2\pi xy)$.

5.2.3 Time-dependent problem

We consider the 2D heat equation as follows:

$$\frac{\partial u}{\partial t} = \alpha \left(\frac{\partial^2 u}{\partial x^2} + \frac{\partial^2 u}{\partial y^2} \right), \quad (x, y) \in [0, 1] \times [0, 1], \quad t \in [0, T], \quad (37)$$

with the initial condition

$$u(x, y, 0) = \sin(\pi x) \sin(\pi y), \quad (x, y) \in [0, 1] \times [0, 1], \quad (38)$$

and the Dirichlet boundary conditions

$$u(x, y, t) = 0, \quad (x, y) \in \partial([0, 1] \times [0, 1]), \quad (39)$$

The exact solution of the above problem is

$$u(x, y, t) = \sin(\pi x) \sin(\pi y) e^{-\alpha 2\pi^2 t}, \quad (x, y) \in [0, 1] \times [0, 1], \quad t \in [0, T]. \quad (40)$$

We assume a final time $T = 0.5$, $\Delta t = 0.005$ and $\alpha = 0.01$. Figure 13 shows the convergence plot for 2D heat equation. The results of the adaptive NN for this test are qualitatively similar to the ones seen in the previous tests. The Hardy, Franke and modified Franke methods produce constant errors, whereas the NN method produces solutions that converge as the number of interpolation points is augmented.

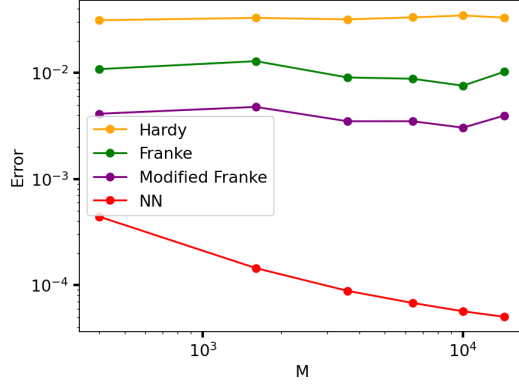


Figure 13: Convergence plot for the 2D heat problem.

We finish this section by presenting the computational cost of our method compared to Hardy’s, Franke’s, modified Franke’s and Rippa’s methods. Tables 3 and 4 show the results for one of the interpolation tasks, in 1-dimension and 2-dimensions, respectively. We present only the results for the interpolation of f_1 and f_4 as there is not much difference between the problems when the dimension and N are fixed. The Hardy, Franke and modified Franke methods are much cheaper to evaluate, whereas the NN method requires a call to the NN for each stencil of size $N = 10$. The Rippa algorithm is by far the most expensive method as it requires the computation of the error vector E over a list of potential shape parameters ε . In the PDE case, the overhead added by the NN method is only at the beginning of the method, as we consider static meshes. In this case, the computational performance of the methods is very similar for sufficiently large number of interpolation points, as most of the computation is on the evolution of the PDE.

Table 3: Comparing computational efficiency between different methods in the 1–dimensional interpolation task (interpolating f_1). The results are reported in seconds.

# Interpolation points	Hardy	Frake	Modified Franke	Rippa	NN
10	3.7e-05	3.2e-06	3.0e-06	2.4e-02	2.2e-03
19	5.0e-05	4.6e-06	3.8e-06	3.5e-02	2.2e-03
37	7.3e-05	6.8e-06	5.5e-06	5.3e-02	3.1e-03
73	1.1e-04	1.0e-05	8.5e-06	8.0e-02	4.7e-03
145	2.0e-04	1.8e-05	1.5e-05	1.5e-01	8.6e-03
289	4.2e-04	3.7e-05	3.0e-05	2.9e-01	1.7e-02
577	8.7e-04	7.6e-05	6.2e-05	6.1e-01	3.6e-02
1153	1.8e-03	1.6e-04	1.3e-04	1.2e+00	7.2e-02
2305	3.4e-03	2.9e-04	2.4e-04	2.3e+00	1.4e-01
4609	7.1e-03	6.2e-04	5.0e-04	4.8e+00	2.9e-01

Table 4: Comparing computational efficiency between different methods in the 2–dimensional interpolation task (interpolating f_4). The results are reported in seconds.

# Interpolation points	Hardy	Frake	Modified Franke	Rippa	NN
20×20	9.1e+00	1.9e+00	1.9e+00	1.7e+02	8.9e+00
40×40	3.7e+01	7.8e+00	7.8e+00	7.0e+02	2.8e+01
60×60	8.2e+01	1.8e+01	1.8e+01	1.6e+03	6.0e+01
80×80	1.5e+02	3.1e+01	3.1e+01	2.8e+03	1.0e+02
100×100	2.3e+02	4.9e+01	4.9e+01	4.3e+03	1.6e+02
120×120	3.3e+02	7.1e+01	7.0e+01	6.3e+03	2.3e+02

5.3 Fallback procedure

In this section, we evaluate numerically the impact of the fallback procedure introduced in Section 4.3.

In Figure 14, we show the error curves for the interpolation of function f_1^4 and f_3 when considering different thresholds, namely $\theta = 12, 16, \infty$. This means that if the NN’s prediction leads to a shape parameter larger than θ , we correct the shape parameter by solving optimisation problem as in Section 3. We note that after the third point ($N = 37$), the fallback procedure is activated when the threshold $\theta = 12$. However, when we increase the threshold to $\theta = 16$, the fallback procedure is no longer activated, meaning that the NN prediction produces shape parameters that lead to interpolation matrices with conditions smaller than 10^{16} . We also note that the error is degraded when we keep the condition of the interpolation matrix to be smaller than 11.5 as the interpolation points get closer together, this is expected as the condition of the interpolation matrix tends to increase as the points get closer to each other.

To try to answer the question of why is the network producing shape parameters that lead to condition numbers outside of the expected range $[10^{11}, 10^{11.5}]$, we hypothesize the flagged datapoints are perhaps out-of-distribution. We plot the distribution of the average of the distance matrix for each input \underline{x} that requires correction, against the average of the distance matrix in the training set, which can be seen in Figure 14 (right) and postulate that these points might be far from the training set points. In Figure 15, we show the same figure for non-equidistant axis and reach similar conclusions.

⁴The error curve for function f_2 is very similar to the one of f_1 and thus is omitted.

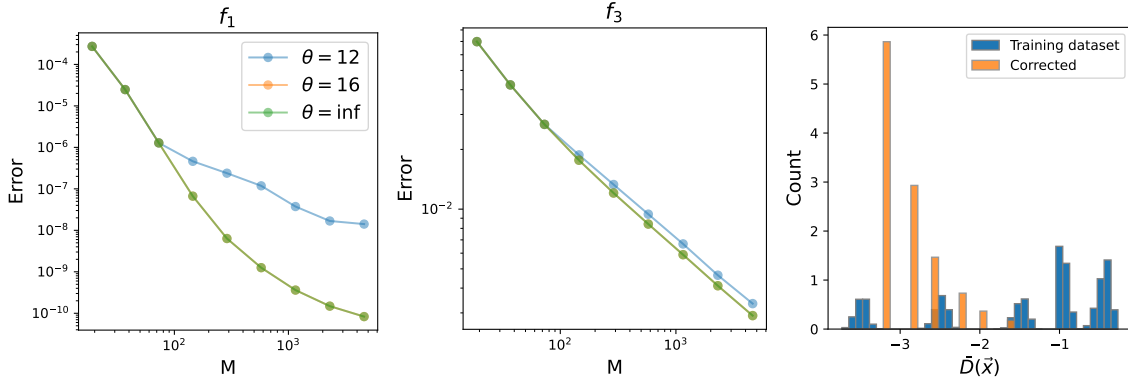


Figure 14: Fallback performance for equidistant interpolation nodes in 1d interpolation tasks. Left: Error convergence plots for functions f_1 and f_3 subject to different thresholds θ . Right: Distribution of the average distance between the corrected points and the training dataset.

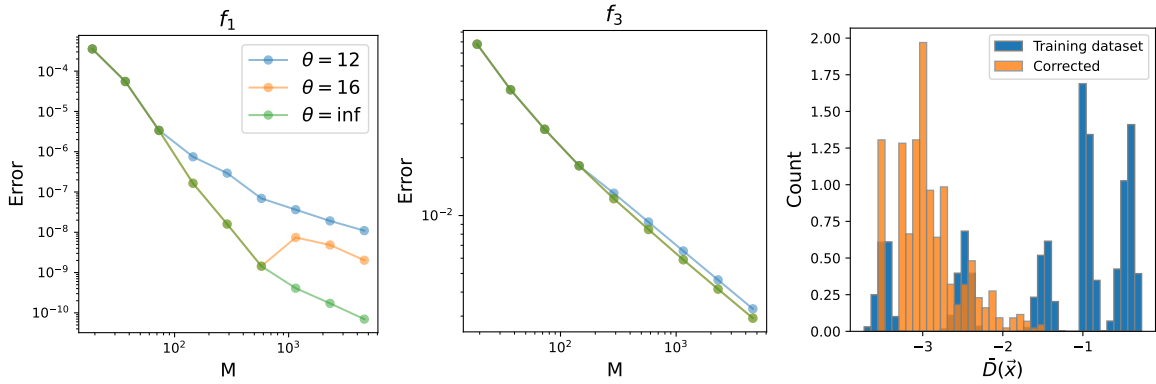


Figure 15: Fallback performance for non-equidistant interpolation nodes in 1d interpolation tasks. Left: Error convergence plots for functions f_1 and f_3 subject to different thresholds θ . Right: Distribution of the average distance between the corrected points and the training dataset.

With this fallback procedure, we have a strong guarantee that the generated interpolation matrix has a controlled condition which can be useful because it places less importance on the creation of the training dataset. For general tasks, we propose to use $\theta = \infty$, which means that the fallback procedure is only activated when the generated interpolation matrix is truly ill-conditioned. The downside to this strategy is that there is significant overhead if the optimisation is required. The performance depends heavily on the initial guess for the optimisation procedure. We currently set the initial guess ε_{init} to be the output of the NN to avoid fine tuning the optimisation procedure, however, the most efficient results we found for the more refined meshes (large M), was to set ε to be high, for example, $\varepsilon_{init} = 400$.

6 Conclusion

In this work, we propose a novel approach to predict a shape parameter for the inverse multiquadric RBFs. The method is based in two parts: i) we derive an optimisation problem that attains a suitable shape parameter for any distribution of points \underline{x} , ii) we use the optimisation problem to generate a dataset and train a NN to predict a suitable shape parameter given any distribution of interpolation points. We focus on a setting where the size of the stencil is fixed and provide a unified strategy for 1–dimensional and 2–dimensional cloud of points. Furthermore, we propose a fallback procedure that guarantees that the generated interpolation matrices (using the predicted shape parameter) remain well-conditioned.

The proposed approach is tested on interpolation tasks and integrated with a RBF-FD method and show promising results in comparison to other adaptive strategies. Although we are able to strictly guarantee the well-posedness of the generated interpolation matrices, there is a computational overhead when further optimisation is necessary. For future work, we will explore continuous learning to retrain the network on unseen examples for which the NN did not produce good enough results. Another future directions is to go towards generalising the strategy to higher dimensions.

Acknowledgments

A Appendix: Dataset generation

Table 5: One-dimension dataset

$u(x)$	Domain	Data per sample
$e^{\sin(\pi x)}$	[0,0.01]	700
	[0,0.1]	700
	[0,1]	700
$\frac{1}{1+16x^2}$	[0,0.01]	700
	[0,0.1]	700
	[0,1]	700
$\cos(200\pi x)$	[0,0.01]	700
$\cos(20\pi x)$	[0,0.1]	700
$\cos(2\pi x)$	[0,1]	700

Table 6: Two-dimension dataset

$u(x, y)$	Domain	# points in domain	Data per sample
$(1 + e^{-\frac{1}{\alpha}} - e^{-\frac{x}{\alpha}} - e^{\frac{(x-1)}{\alpha}})(1 + e^{-\frac{1}{\alpha}} - e^{-\frac{y}{\alpha}} - e^{\frac{(y-1)}{\alpha}})$ $\alpha = 0.1$	[0,0.001] [0,0.01] [0,0.1] [0,1]	20 20 20 20	50 50 50 50
$(1 + e^{-\frac{1}{\alpha}} - e^{-\frac{x}{\alpha}} - e^{\frac{(x-1)}{\alpha}})(1 + e^{-\frac{1}{\alpha}} - e^{-\frac{y}{\alpha}} - e^{\frac{(y-1)}{\alpha}})$ $\alpha = 1$	[0,0.001] [0,0.01] [0,0.1] [0,1]	20 20 20 20	50 50 50 50
$\frac{3}{4}e^{-\left(\frac{(9x-2)^2+(9y-2)^2}{4}\right)} + \frac{3}{4}e^{-\left(\frac{(9x+1)^2+(9y+1)^2}{49} + \frac{(9y+1)^2}{10}\right)}$ $+ \frac{1}{2}e^{-\left(\frac{(9x-7)^2+(9y-3)^2}{4}\right)} - \frac{1}{5}e^{-\left((9x-4)^2+(9y-7)^2\right)}$	[0,0.001] [0,0.01] [0,0.1] [0,1]	20 20 20 20	50 50 50 50

Algorithm 2: Generate dataset

Input: Desired interval $[a, b]$, the number of points N in the interval, learning rate and number of data per sample

Output: a set of sorted N data points $\underline{x} = (x_1, \dots, x_N)$ with corresponding shape parameter

- Generate uniformly distributed sample \underline{x}
- Initialize the shape parameter with $\varepsilon = \frac{1}{0.815N \sum_{i=1}^N d_i}$, where d_i is the distance between the the i -th data point and its nearest neighbour
- Set trials = 0
- Set unsuccessful = 0
- while** $loss > 10^{-3}$ **do**
 - Solve (19) using Adam stochastic optimizer
 - trials = trials + 1
 - if** trials > 40 **then**
 - unsuccessful = 1
 - break
 - end**
- end**
- if** unsuccessful = 0 **then**
 - | Add \underline{x} with corresponding shape parameter ε to the dataset
- end**

References

- [1] H. Wendland. *Scattered data approximation*. Cambridge Monographs on Applied and Computational Mathematics. Cambridge University Press, 2004.
- [2] R.E. Carlson and T.A. Foley. The parameter R2 in multiquadric interpolation. *Computers & Mathematics with Applications*, 21(9):29–42, 1991.
- [3] R.L. Hardy. Multiquadric equations of topography and other irregular surfaces. *Journal of geophysical research*, 76(8):1905–1915, 1971.

- [4] R. Franke. Scattered data interpolation: tests of some methods. *Mathematics of computation*, 38(157):181–200, 1982.
- [5] L.H. Kuo. On the selection of a good shape parameter for rbf approximation and its application for solving pdes. *The University of Southern Mississippi*, 2015.
- [6] T.A. Foley. Interpolation and approximation of 3-d and 4-d scattered data. *Computers & Mathematics with Applications*, 13(8):711–740, 1987.
- [7] E.J. Kansa and R.E. Carlson. Improved accuracy of multiquadric interpolation using variable shape parameters. *Computers & Mathematics with Applications*, 24(12):99–120, 1992.
- [8] S. Rippa. An algorithm for selecting a good value for the parameter c in radial basis function interpolation. *Advances in Computational Mathematics*, 11:193–210, 1999.
- [9] M.A. Golberg, C.S. Chen, and S.R. Karur. Improved multiquadric approximation for partial differential equations. *Engineering Analysis with Boundary Elements*, 18(1):9–17, 1996.
- [10] M. Scheuerer. An alternative procedure for selecting a good value for the parameter c in rbf-interpolation. *Advances in Computational Mathematics*, 34(1):105–126, 2011.
- [11] F. Marchetti. The extension of rippa’s algorithm beyond loocv. *Applied Mathematics Letters*, 120:107262, 2021.
- [12] L. Ling and F. Marchetti. A stochastic extended rippa’s algorithm for lpocv. *Applied Mathematics Letters*, 129:107955, 2022.
- [13] B. Fornberg and J. Zuev. The runge phenomenon and spatially variable shape parameters in rbf interpolation. *Computers & Mathematics with Applications*, 54(3):379–398, 2007.
- [14] G.E. Fasshauer and J.G. Zhang. On choosing “optimal” shape parameters for rbf approximation. *Numerical Algorithms*, 45:345–368, 2007.
- [15] G.B. Wright. *Radial basis function interpolation: numerical and analytical developments*. PhD thesis, University of Colorado at Boulder, 2003.
- [16] B. Fornberg and G. Wright. Stable computation of multiquadric interpolants for all values of the shape parameter. *Computers & Mathematics with Applications*, 48(5):853–867, 2004.
- [17] F.N. Mojarrad, M.H. Veiga, J.S. Hesthaven, and P. Öffner. A new variable shape parameter strategy for rbf approximation using neural networks. *Computers & Mathematics with Applications*, 143:151–168, 2023.
- [18] N. Flyer, B. Fornberg, V. Bayona, and G.A. Barnett. On the role of polynomials in RBF-FD approximations: I. interpolation and accuracy. *Journal of Computational Physics*, 321:21–38, 2016.

- [19] A.I. Tolstykh and D.A. Shirobokov. On using radial basis functions in a “finite difference mode” with applications to elasticity problems. *Computational Mechanics*, 33(1):68–79, 2003.
- [20] I. Tominec and E. Breznik. An unfitted RBF-FD method in a least-squares setting for elliptic pdes on complex geometries. *Journal of Computational Physics*, 436:110283, 2021.
- [21] P.K. Mishra, G.E. Fasshauer, M.K. Sen, and L. Ling. A stabilized radial basis-finite difference (RBF-FD) method with hybrid kernels. *Computers & Mathematics with Applications*, 77(9):2354–2368, 2019.
- [22] G.B. Wright and B. Fornberg. Scattered node compact finite difference-type formulas generated from radial basis functions. *Journal of Computational Physics*, 212(1):99–123, 2006.
- [23] R. Schaback. Error estimates and condition numbers for radial basis function interpolation. *Advances in Computational Mathematics*, 3(3):251–264, 1995.
- [24] G.E. Fasshauer. *Meshfree Approximation Methods with MATLAB*. World Scientific, 2007.
- [25] T.A. Driscoll and B. Fornberg. Interpolation in the limit of increasingly flat radial basis functions. *Computers & Mathematics with Applications*, 43(3-5):413–422, 2002.
- [26] S. Barthelmé and K. Usevich. Spectral properties of kernel matrices in the flat limit. *SIAM Journal on Matrix Analysis and Applications*, 42(1):17–57, 2021.
- [27] Maria Han Veiga and Fatemeh Nassajian Mojarrad. Robust rbf shape parameter github. <https://github.com/hanveiga/RBF-shape-parameter-NN>, 2024.
- [28] A. Lee, J.H. Ghouse, J.C. Eslick, C.D. Laird, J.D. Sirola, M.A. Zamarripa, D. Gunter, J.H. Shinn, A.W. Dowling, D. Bhattacharyya, L.T. Biegler, A.P. Burgard, and D.C. Miller. The idaes process modeling framework and model library—flexibility for process simulation and optimization. *Journal of Advanced Manufacturing and Processing*, 3(3):e10095, 2021.
- [29] C. W. Gear. The numerical integration of ordinary differential equations. *Mathematics of Computation*, 21(98):146—156, 1967.
- [30] G.E. Fasshauer. Newton iteration with multiquadrics for the solution of nonlinear pdes. *Computers & Mathematics with Applications*, 43(3-5):423–438, 2002.
- [31] G.E. Fasshauer, E.C. Gartland, and J.W. Jerome. Newton iteration for partial differential equations and the approximation of the identity. *Numerical Algorithms*, 25(1):181–195, 2000.
- [32] M.A. Jankowska, A. Karageorghis, and C.S. Chen. Improved Kansa RBF method for the solution of nonlinear boundary value problems. *Engineering Analysis with Boundary Elements*, 87:173–183, 2018.